JFM RAPIDS
journals.cambridge.org/rapids

Direct simulation of surface roughness signature of internal wave with deterministic energy-conservative model

Xuanting Hao[1] and Lian Shen[1,†]

[1]Department of Mechanical Engineering, and St. Anthony Falls Laboratory, University of Minnesota, Minneapolis, MN 55455, USA

In this simulation-based study, we investigate the surface roughness signature induced by internal solitary waves in oceans. We present the first-ever effort to directly capture the surface roughness signature with a deterministic two-layer model to avoid the singularity encountered in the traditional wave–current interaction theory. By capturing over four million wave components, the simulation resolves the surface wave and internal wave dynamics simultaneously. The surface signature characterized by a rough region followed by a smooth region travelling with an internal wave is quantified by the local wave geometry variation and the wave energy change. The surface wave dynamics are analysed in the wavenumber–frequency slope spectrum calculated in the frame moving with the internal wave. The asymmetric behaviours of right-moving and left-moving surface waves are found to contribute to the surface signature formation. Our results show that the formation of the surface signature is essentially an energy-conservative process and justify the use of the wave-phase-resolved two-layer model.

Key words: surface gravity waves, internal waves, solitary waves

1. Introduction

As internal waves propagate, they leave on the ocean surface a distinct signature of alternating rough and smooth regions. When observed using satellite radars, this signature of internal waves appears in the form of bright and dark bands, similar to the white and black stripes of a zebra. Such bands appear because a spatial change in the wave roughness induces a variation in the strength of the backscattering of the electromagnetic signals of radars (Perry & Schimke 1965; Ziegenbein 1969; Osborne & Burch 1980). The surface signature obtained via remote sensing is a critical technique for the identification of internal waves (Helfrich & Melville 2006), which allows a large area coverage compared with *in situ* measurements. The heterogeneity

† Email address for correspondence: shen@umn.edu

in surface roughness can impact the physical properties of the near-surface atmosphere (Ortiz-Suslow *et al.* 2019). Despite its importance, it remains a challenge to quantify the surface signature induced by internal waves. It is desirable to resolve a wide range of wave motions from the first principles of fluid dynamics so that the impact of internal waves on the surface waves can be accurately described and modelled.

In previous studies, attempts to quantify the surface wave variation are often based on the ray theory, which is similar to geometrical optics. In this theory, an individual surface wave component is tracked by the change in its wavenumber and energy, whereas the wave phase is discarded. The effect of the internal wave is generally treated as a prescribed time-invariant surface current (Alpers 1985; Donato, Peregrine & Stocker 1999; Bakhanov & Ostrovsky 2002). Under this assumption, a singularity occurs when the surface waves are blocked by the countercurrent induced by the internal wave (Peregrine 1976). The singularity can be illustrated by the dispersion relation of a one-dimensional surface wave in a current, $\omega = kU + \sqrt{gk}$, where ω denotes the wave (angular) frequency, k the wavenumber and U the current velocity. The dispersion relation is therefore a quadratic equation for $\sqrt{k}$. If the wave and current are counterpropagating, i.e. $kU < 0$, and if the current is sufficiently strong, it is possible that the equation has no real solutions where the wave is blocked by the current (Smith 1975; Peregrine 1976). For certain idealized wave conditions, the wave amplitude can be approximated by an Airy function in the vicinity of the blocking point (Smith 1975; Peregrine 1976; Nardin, Rousseaux & Coullet 2009). For the more complex surface signature formation, the explanation based on the ray theory contrasts with the conservative mechanism that involves the surface wave absorption and reflection, according to Craig, Guyenne & Sulem (2012).

Furthermore, it remains unclear whether external physical processes play a determining role in the surface signature formation. Surface waves can acquire energy from wind and dissipate energy via turbulent motions when they break. Because these processes may also affect the water surface roughness (Bakhanov & Ostrovsky 2002; Jackson, Silva & Jeans 2013), some studies based on the ray theory include them in the governing equation (e.g. Alpers 1985; Bakhanov & Ostrovsky 2002). Others choose to exclude the effects of wind and wave breaking and isolate the effect of internal waves using numerical simulation and laboratory measurement. For example, Craig *et al.* (2012) derived a system of a coupled Korteweg–de Vries (KdV) equation and a Schrödinger equation based on the two-layer ocean model to describe the dynamics of long internal waves and surface waves, which was then used to study surface waves near a carrier wavenumber. Similarly, Jiang *et al.* (2019) developed a Boussinesq-type model from the two-layer model for the modelling of the coupled internal wave and surface wave field and investigated the asymmetric behaviour of long surface waves. Kodaira *et al.* (2016) conducted a laboratory measurement in the two-layer setting and observed short surface waves travelling at approximately the same speed as the internal wave. While not directly showing the zebra pattern, these studies suggest that an internal wave can induce the surface signature in the absence of wind input and wave breaking.

In this work, we show that the surface signature can be formed within an energy-conservative framework, from which the singularity in the ray theory and the effect of external processes are excluded. Our study is based on the simulation of a two-layer fluid model (Lamb 1932; Sutherland 2010). Starting from the wave-phase-resolved governing equations allows us to avoid the singularity issue encountered in the phase-averaging ray theory. This approach is justified by a number of studies in the astrophysics community (e.g. Schützhold & Unruh 2002; Euvé *et al.* 2015), which use the blocking events in wave–current interaction as an analogue to

the black hole physics. Under the potential flow assumption, the simulation framework conserves energy (Alam, Liu & Yue 2009*a*; Tanaka & Wakayama 2015), and thus the interaction between surface waves and internal waves is isolated from the effects of external energy sources.

The remainder of this paper is organized as follows. In § 2, we briefly review the mathematical model and introduce the problem set-up. In § 3, we present the observation and analysis of the surface signature. Finally, discussions and conclusions are given in § 4.

2. Methodology

2.1. *Mathematical model*

In this study, we use a deterministic wave-phase-resolved model to address the major challenge in quantifying the surface signature: capturing the broadband wave motions between two distinct length scales. The first one is the length scale of the surface waves relevant to the zebra pattern observed by satellite radars, which can be inferred from the radar electromagnetic signal wavelength, ranging from a few centimetres to a few decimetres (Martin 2014), because water waves are visible to the radar signal only when their wavelengths are close such that the Bragg scattering can occur. On the surface gravity wave spectrum (Munk 1950), these surface waves are located near the gravity–capillary wave boundary. The second length scale is that of internal waves, which often span several hundred metres or several kilometres (Perry & Schimke 1965). As pointed out by Jiang *et al.* (2019), the short surface wave motions are not resolved in their study because a long-wave approximation is used in the Boussinesq-type wave-phase-resolving model. In our numerical simulation, the wave motions at these two distinct length scales are directly captured with a sufficiently large number of wave modes.

Our simulation is performed using the two-layer ocean model based on the potential flow assumption (Lamb 1932; Sutherland 2010) (see also the supplementary material, available at https://doi.org/10.1017/jfm.2020.200). The fluid motions in both layers, assumed to be inviscid, incompressible and irrotational, are governed by the Laplace equation in terms of the velocity potential. We also assume that the fluids are immiscible at the interface and that the vertical velocity vanishes at the bottom of the lower layer. Using the surface/interface elevations and velocity potentials, one can derive a group of evolution equations based on the fully nonlinear kinematic and dynamic boundary conditions at the surface and interface as follows (note that the form of these equations is different from the original boundary conditions because of the surface and interface quantities used; for details, see Alam, Liu & Yue (2009*b*)):

$$\frac{\partial \eta_u}{\partial t} = -\nabla \eta_u \cdot \nabla \phi_u^s + (1 + |\nabla \eta_u|^2)\phi_{u,z}, \tag{2.1}$$

$$\frac{\partial \phi_u^s}{\partial t} = -g\eta_u - \frac{1}{2}|\nabla \phi_u^s|^2 + \frac{1}{2}(1 + |\nabla \eta_u|^2)\phi_{u,z}^2 + \frac{\sigma_s}{\rho_u}\nabla \cdot \left[\frac{\nabla \eta_u}{\sqrt{1 + |\nabla \eta_u|^2}}\right], \tag{2.2}$$

$$\frac{\partial \eta_l}{\partial t} = -\nabla \eta_l \cdot \nabla \phi_u^i + (1 + |\nabla \eta_l|^2)\phi_{u,z}, \tag{2.3}$$

$$\frac{\partial \psi^i}{\partial t} = \frac{1}{2}(R|\nabla \phi_u^i|^2 - |\nabla \phi_l^i|^2) - g\eta_l(1 - R) + \frac{1}{2}(1 + |\nabla \eta_l|^2)(\phi_{l,z}^2 - R\phi_{u,z}^2)$$

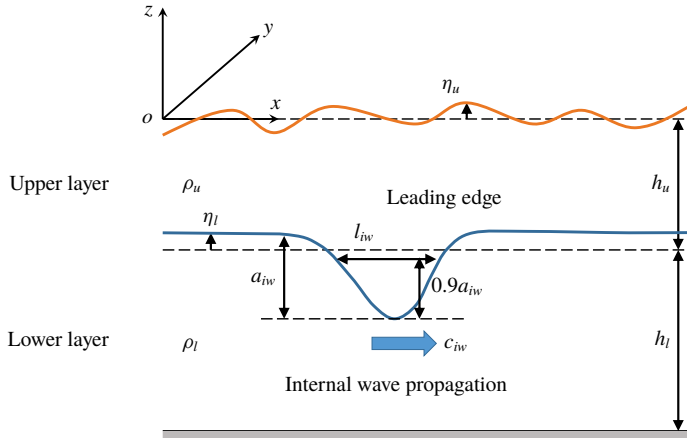$$+ \frac{\sigma_i}{\rho_l}\nabla \cdot \left[\frac{\nabla \eta_l}{\sqrt{1 + |\nabla \eta_l|^2}}\right], \tag{2.4}$$

FIGURE 1. Sketch of interaction between surface waves and an internal solitary wave in a two-layer model.

where ϕ_u (respectively, ϕ_l), ρ_u (respectively, ρ_l) and h_u (respectively, h_l) are the velocity potential, density and mean depth of the upper (respectively, lower) layer fluid, σ_s (respectively, σ_i) is the surface tension of the air–upper fluid surface (respectively, upper–lower fluid interface), $\nabla = (\partial/\partial x, \partial/\partial y)$ denotes the gradient operator in the horizontal directions, $\phi_u^s(\boldsymbol{x}, t) = \phi_u(\boldsymbol{x}, \eta_u(\boldsymbol{x}, t), t)$, $\psi^i(\boldsymbol{x}, t) = \phi_l^i(\boldsymbol{x}, t) - R\phi_u^i(\boldsymbol{x}, t)$ and $R = \rho_u/\rho_l$ is the density ratio (figure 1). These equations are solved based on the perturbation expansion of the surface/interface quantities. The calculation of the surface tension is valid when η_u and η_l are single-valued functions, provided that the wave steepness is not too large to induce wave breaking.

2.2. *Simulation set-up*

The numerical experiment, based on a high-order spectral method (Alam *et al.* 2009*b*), is outlined here. The evolution equations are discretized on a uniform grid in a rectangular domain with periodic boundary conditions and then integrated in time to obtain the evolution of the wave fields. The initial condition is a superposition of the eigenfunctions of the linearized two-layer system, i.e. wave-like solutions of barotropic mode and baroclinic mode, and then nonlinear waves develop and evolve dynamically in the simulation. Our numerical code has been validated by repeating the simulations of the classical nonlinear wave interaction in a single resonant triad (Alam *et al.* 2009*b*) and a broadband spectrum (Tanaka & Wakayama 2015). Additionally, we have conducted an auxiliary test case, for which the parameters are adapted from a recent laboratory measurement (Kodaira *et al.* 2016); the details of validation can be found in Hao (2019).

In the main computational case of the present study, the key physical parameters are comparable to a typical internal wave observed in the field (Stanton & Ostrovsky 1998). Specifically, the upper layer depth is approximated by the pycnocline depth of the observation, while the lower layer depth is the same as the model variable used in their simulation. The initial amplitudes of the surface wave components are set based on the observational data at station 5 in the Joint North Sea Wave Project (JONSWAP) (see figure 2.5 in Hasselmann *et al.* (1973)). Note that the spectrum decays rapidly in the low-wavenumber limit and the energy density for waves longer

$(h_u,\ h_l)$ (m)	$(L_x,\ L_y)$ (m)	$(N_x,\ N_y)$	Δ_e (m)	λ_e (m)
(7, 140)	(500, 125)	(6144, 1536)	0.12	0.24
a_{iw} (m)	c_{iw} (m s^{-1})	l_{iw} (m)	λ_p (m)	c_p (m s^{-1})
-5	0.52	154	10	3.9
$R = \rho_u/\rho_l$	h_u/h_l	$Fr = c_p/\sqrt{gh_u}$	$Re = c_p\lambda_p/\nu$	$We(Bo) = \rho_u g/\sigma_s k_e^2$
0.997	0.05	0.48	∞	195

TABLE 1. Physical and computational parameters of the simulation: h_u and h_l are the mean depth of the upper and lower fluid, respectively; L_x and L_y are the computational domain size in the x and y directions, respectively; N_x and N_y are the corresponding grid numbers; $\Delta_e = 1.5L_x/N_x = 1.5L_y/N_y$ is the effective grid size after considering dealiasing; λ_e is the wavelength of the shortest wave resolved; a_{iw} is the internal wave amplitude, with the negative sign denoting a depression wave; c_{iw} is the internal wave phase velocity; l_{iw} is the internal wave width defined at 90 % amplitude (see figure 1); λ_p is the peak surface wavelength; c_p is the peak surface wave phase velocity; ν is the viscosity, which vanishes under the inviscid flow assumption; and $\sigma_s = 0.073$ N m^{-1} is the surface tension at the air–water interface. Also listed are the non-dimensional numbers: the density ratio, the layer depth ratio, the Froude number, the Reynolds number and the Weber/Bond number, respectively.

than $3\lambda_p$ is less than 0.8 % of the peak wave energy. Therefore, the total depth is sufficiently deep for the surface waves. The weight of the wave energy propagating in each direction is specified by the directional spreading function $D(\theta) = (2/\pi) \cos^2 \theta$, where θ is the angle between the wave propagation direction and the x axis (Young 1999). A random number is assigned to the initial phase of each wave component. The initial baroclinic (internal) wave components are extracted from a permanent form of internal wave solution of the KdV equation (see the review by Helfrich & Melville (2006)). The computational domain is rectangular and sufficiently large to cover the internal wave. After considering the aliasing error, the total number of wave modes is approximately 4.2×10^6, nearly 24 times that in the simulation of Tanaka & Wakayama (2015). The initial condition is then generated with the information of wave amplitude for the barotropic wave modes and baroclinic wave modes. The Weber (Bond) number corresponding to the shortest resolved wave is high (table 1), suggesting that the surface tension forces are negligibly small. Therefore, the associated terms are not computed for the consideration of simulation time. The time-step size is $0.028T_p$, approximately 18 % of the period of the shortest wave resolved. The simulation is performed for a duration of about $83T_p$. The physical and computational parameters are presented in table 1.

3. Results

3.1. *Direct observation of surface signature*

The surface signature can be directly observed from the surface elevation with the naked eye (Woodson 2018). In our simulation, the initial surface wave field is statistically homogeneous and the surface signature is found to form gradually and maintain throughout the simulation. We present an example of the instantaneous surface elevation and the interface elevation in figure 2(*a*). As shown, a rough surface region with increased wave steepness is formed above the leading edge of the internal wave (figure 1). Right behind the rough region there is a smooth region where the
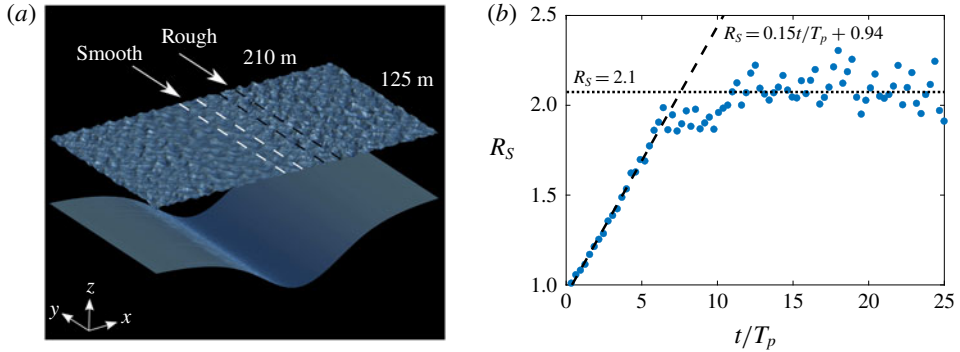
FIGURE 2. (*a*) Direct observation of the surface signature, denoted by the instantaneous surface wave elevation field. (*b*) Temporal evolution of the steepness ratio. In (*a*), also shown are the interface elevation and the boundaries of the regions used for spectral analysis in § 3.3, denoted by dashed lines. For clarity, we only plot part of the computational domain. The internal wave propagates in the $+x$ direction. In (*b*), two trendlines are plotted.

surface wave steepness is significantly reduced. The rough and smooth regions correspond to a pair of bright and dark bands on satellite images. Qualitatively, the surface signature observed in the present study shows several key features in remote sensing observations, including the location of the rough and smooth regions with respect to the internal wave, their length scales and the propagating speed. For the purpose of quantitative comparison with observational data, the wave-phase-resolved surface signature can potentially be valuable by providing hydrodynamic information to radar electromagnetic signal simulations (e.g. Liu & He 2016; Yoshida 2017), which were conducted on artificially generated ocean surfaces in the literature.

The formation of the surface signature is a transient process, during which the initially homogeneous surface waves respond to the time-varying surface strain field driven by the internal wave. To illustrate this process, we define the density ratio $R_S = \int S_{rough} \, dx \, dy / \int S_{smooth} \, dx \, dy$, where $S(x, y) = [(\partial \eta_u / \partial x)^2 + (\partial \eta_u / \partial y)^2]^{1/2}$ is the local steepness and the integrations are performed in the regions denoted by the dashed lines in figure 2(*a*). As shown in figure 2(*b*), R_S first undergoes a transient, linear growth stage (dashed line) and then settles around 2.1 (dotted line). The time scale of the transient process is approximately $7.7T_p$, which is much shorter than the time scale of the internal wave: $l_{iw}/c_{iw} = 117T_p$. Therefore, for a fixed point in the Eulerian frame, we expect the surface wave energy to undergo a rapid transient process as the time-varying surface strain field driven by the internal solitary wave as it passes by.

3.2. *Quantitative analysis of surface signature*

To quantify the roughness change, we calculate the local steepness (figure 3*a*) and find that the wave steepness in the rough region is higher than that in the smooth region in a statistical sense. As shown in figure 3(*b*), the surface wave energy change $\Delta E/E_0$ calculated from the wavenumber spectrum can also reveal the surface signature pattern. We divide the computational domain into 48 regions along the x direction, each with a size of 10.4 m $\times$ 125 m. Then we conduct a two-dimensional Fourier transform on the product of the surface elevation $\eta_u(x, y)$ and a window function in each region
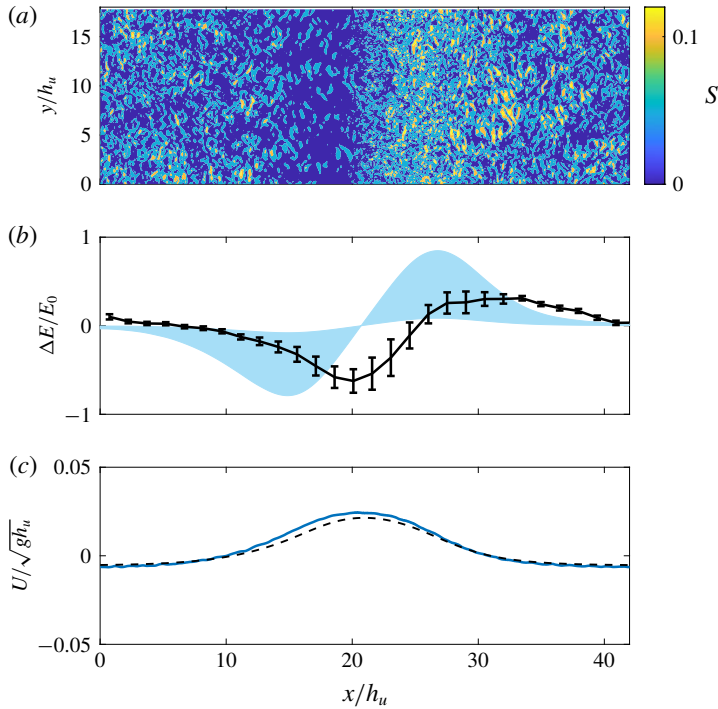
FIGURE 3. Quantitative analysis of the surface signature. (*a*) Plan view of the instantaneous local steepness $S = [(\partial\eta_u/\partial x)^2 + (\partial\eta_u/\partial y)^2]^{1/2}$ of the surface wave field, where η_u is the surface elevation. (*b*) The change in surface wave energy ΔE normalized by the unperturbed value E_0, where the black solid line denotes the mean value over all wavenumbers and the error bar denotes the standard deviation. The shaded area in light blue denotes the range of the empirical estimation (Alpers 1985). (*c*) Surface current induced by the internal wave. Our numerical result is denoted by the blue solid line and the first-order approximation is denoted by the black dashed line.

and obtain the wavenumber spectrum $E(k_x, k_y)$. Considering that the surface wave field should be statistically homogeneous in the y direction, we perform averaging to obtain the one-dimensional wavenumber spectrum $E(k_x) = \int E(k_x, k_y)\,\mathrm{d}k_y$.

To clarify the correlation between the wave energy change and the surface motion induced by the internal wave, we provide another estimation according to the formula proposed by Alpers (1985): $\Delta E/E_0 = -\tau\,\mathrm{d}U/\mathrm{d}x$, where $\tau = 21.2$–212 s is a relaxation time set empirically based on the time scale of the surface wave energy transfer processes including wind input, nonlinear interaction and dissipation and $\mathrm{d}U/\mathrm{d}x$ is the gradient of the surface current. Overall, the results are consistent and show the same trend in the wave energy change, which sees an apparent correlation with the current gradient (figure 3*b*). Here the surface current is calculated by performing averaging in the spanwise direction and time averaging in the reference frame moving with the internal wave. The gradient of the current $\mathrm{d}U/\mathrm{d}x$ is then calculated from $U(x)$. Instead of direct calculation with a finite difference approximation, we compute $\mathrm{d}U/\mathrm{d}x$ by minimizing a functional to avoid extreme values caused by irregularity and noise in $U(x)$ (Chartrand 2011). The first-order approximation of the current can also be estimated from mass conservation: $-c_{iw}\eta_l/(h_u - \eta_l)$. Overall, the two results
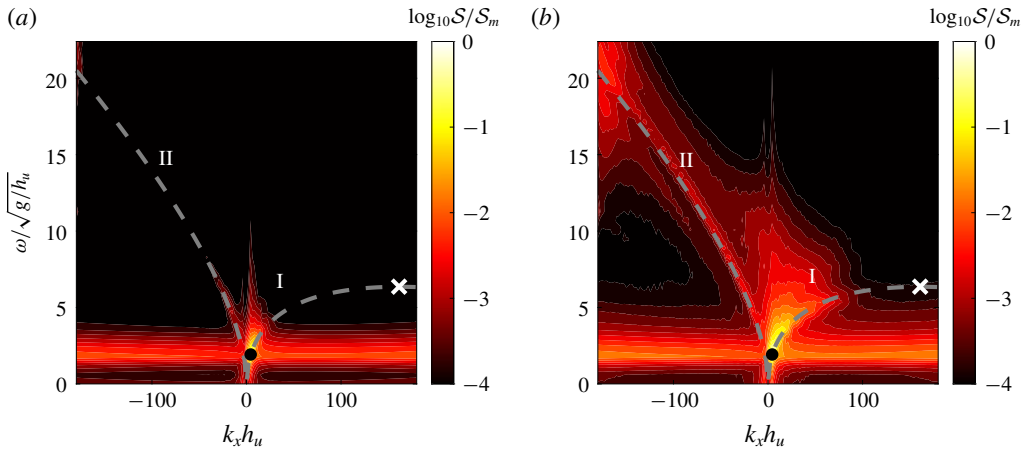
FIGURE 4. Wavenumber–frequency slope spectrum of surface waves in the (*a*) smooth region and (*b*) rough region. The spectrum is normalized by the maximum value $\mathcal{S}_m$. The dashed curves denote the dispersion relation of the surface waves in the moving frame of reference: $\omega = (U_m - c_{iw})k_x + \sqrt{g|k_x|}$, where U_m is the maximum value of the surface current U (see figure 3). The white cross denotes the maximum frequency of the right-moving surface wave $\omega_m = -g/4(U_m - c_{iw})$. The black filled circle denotes the peak surface wave. The asymmetric behaviours of the surface waves mostly occur in zones I and II.

agree with each other except for small deviations in the region above the internal wave trough (figure 3*c*).

3.3. *Surface waves in the wavenumber–frequency domain*

To elucidate the formation of the surface signature, we conduct spectral analysis on the surface elevation in the frame of reference travelling with the internal wave. The data are extracted from two domains above the internal wave trough, one in the smooth region and the other in the rough region (see the dashed lines in figure 2*a*). The size of each subdomain is 21 m × 125 m, smaller than the actual length scale of the smooth and rough regions to ensure the homogeneity requirement in Fourier analysis. The wavenumber–frequency spectrum $E(k_x, k_y, \omega)$ of surface elevation is then calculated in each subdomain. To better reveal the roughness change of the surface wave field, we further calculate the slope spectrum $\mathcal{S}(k_x, k_y, \omega) = (k_x^2 + k_y^2)E$. In the following analysis, the integrated spectrum $\mathcal{S}(k_x, \omega) = \int \mathcal{S}(k_x, k_y, \omega)\, dk_y$ is presented for clarity. In terms of the physical meaning, the slope spectrum $\mathcal{S}(k_x, k_y, \omega)$ can be seen as the spectral space counterpart to the steepness function $S(x, y)$ in figure 3(*a*).

From the contours of the wavenumber–frequency spectra (figure 4), we can separately identify the energy associated with the two different eigenfunctions in the internal wave system: the baroclinic mode energy is located in the low-frequency portion, while the barotropic mode energy is primarily along the dispersion relation curve of the surface wave in the moving frame of reference as shown by the dashed lines. Because of the space and time limits of the domain used for Fourier analysis, the wave components of low frequency, e.g. $\omega/\sqrt{g/h_u} \sim O(3)$, appear as white-noise-like bands on the spectrum. In the moving frame, the surface motion induced by the internal wave is a countercurrent because $U - c_{iw} < 0$. As a result,

there exists a maximum frequency $\omega_m = -g/4(U_m - c_{iw})$ for surface waves propagating against the current (Donato *et al.* 1999; Nardin *et al.* 2009).

The surface signature can be identified from the asymmetric behaviours of the surface waves. In the rough region, we observe a distinct difference in both right-moving and left-moving surface waves (see zones I and II in figure 4*b*) compared with those in the smooth region (figure 4*a*). Let δS (respectively, δE) denote the difference of the slope (respectively, energy) spectrum between the rough and smooth region and we have $\delta S = k^2 \delta E$. The wave energy change in zone I is larger than that in zone II, i.e. $\delta E_I > \delta E_{II}$, because the background surface wave energy is maximal near the peak wave component (see the black filled circle in figure 4). Meanwhile, the wavenumber of wave components in zone II, especially those shorter than $O(1\ \text{m})$, or $k_x h_u < O(50)$, is higher than that in zone I, namely, $k_I < k_{II}$. Overall, the contribution of the zone II waves to the roughness change is comparable to that of zone I waves, i.e. $\delta S_{II} \sim \delta S_I$.

The asymmetric behaviours of the right-moving surface waves in zone I, such as the increased magnitude towards the leading edge of the internal wave, are consistent with previous studies (Bakhanov & Ostrovsky 2002; Kodaira *et al.* 2016; Jiang *et al.* 2019). In contrast, there are no previous studies reporting the contribution of the left-moving surface waves of small length scales in zone II, because short surface wave dynamics were usually neglected. For example, Jiang *et al.* (2019) studied surface waves yielding the long-wave (shallow-water) approximation, which assumes that the surface wavelength scales are much greater than the fluid layer thickness. Even for the peak surface waves $k_x h_u \approx 4.4$, the upper layer fluid can still be viewed as deep water (e.g. Dean & Dalrymple 1991).

4. Conclusions

In this study, we have performed the first simulation to directly capture the surface roughness signature induced by an internal wave using a deterministic phase-resolved two-layer fluid model. A realistic setting for the interaction between a broadband surface wave field and a typical oceanic internal wave is considered. The wave dynamics of nearly 4.2×10^6 independent components are resolved, covering the wide range of length scales between the internal wave and short surface waves.

Our results show that the formation of the surface signature is essentially an energy-conservative process. In other words, energy sources and sinks, including wind input and wave breaking, are not necessarily the direct cause of the surface signature. With the surface wave and internal wave dynamics captured, the surface signature is quantified using the wave geometry and the energy change. For the first time, the roughness change is identified on the full wavenumber–frequency slope spectrum in a realistic ocean setting of internal and surface waves, which substantiates the contribution of the asymmetric behaviours of the right-moving surface waves to the roughness change. Moreover, our result shows that left-moving waves shorter than $O(1\ \text{m})$ also play an important role in the surface signature formation.

Admittedly, we have neglected the effects of the stratification associated with the continuous density profile, turbulence and the stronger nonlinearity in internal waves. For example, the internal wave amplitude in the present computational case is smaller than that in the original field observation (Stanton & Ostrovsky 1998). Consequently, the magnitude of the surface current induced by the internal wave and thus the roughness change may be underestimated. In future study, the stratification effects can also be captured by solving the full three-dimensional Navier–Stokes equations, yet at a considerably high computational cost not affordable with the current computing power.

Acknowledgements

Declaration of interests

The authors report no conflict of interest.

Supplementary material and movies

Supplementary material and movies are available at https://doi.org/10.1017/jfm.2020.200.

References

ALAM, M.-R., LIU, Y. & YUE, D. K. P. 2009*a* Bragg resonance of waves in a two-layer fluid propagating over bottom ripples. Part I. Perturbation analysis. *J. Fluid Mech.* **624**, 191–224.

ALAM, M.-R., LIU, Y. & YUE, D. K. P. 2009*b* Bragg resonance of waves in a two-layer fluid propagating over bottom ripples. Part II. Numerical simulation. *J. Fluid Mech.* **624**, 225–253.

ALPERS, W. 1985 Theory of radar imaging of internal waves. *Nature* **314**, 245–247.

BAKHANOV, V. V. & OSTROVSKY, L. A. 2002 Action of strong internal solitary waves on surface waves. *J. Geophys. Res.: Oceans* **107** (C10), 3139.

CHARTRAND, R. 2011 Numerical differentiation of noisy, nonsmooth data. *ISRN Applied Mathematics* **2011**, 164564.

CRAIG, W., GUYENNE, P. & SULEM, C. 2012 The surface signature of internal waves. *J. Fluid Mech.* **710**, 277–303.

DEAN, R. G. & DALRYMPLE, R. A. 1991 *Water Wave Mechanics for Engineers and Scientists*. World Scientific.

DONATO, A. N., PEREGRINE, D. H. & STOCKER, J. R. 1999 The focusing of surface waves by internal waves. *J. Fluid Mech.* **384**, 27–58.

EUVÉ, L. P., MICHEL, F., PARENTANI, R. & ROUSSEAUX, G. 2015 Wave blocking and partial transmission in subcritical flows over an obstacle. *Phys. Rev.* D **91** (2), 024020.

HAO, X. 2019 A song of atmosphere and ocean: modeling and simulation-based study of nonlinear waves. PhD thesis, University of Minnesota, Minneapolis, MN.

HASSELMANN, K., BARNETT, T. P., BOUWS, E., CARLSON, H., CARTWRIGHT, D. E., ENKE, K., EWING, J. A., GIENAPP, H., HASSELMANN, D. E., KRUSEMAN, P. *et al.* 1973 *Measurements of Wind-Wave Growth and Swell Decay During the Joint North Sea Wave Project (JONSWAP)*. Deutsches Hydrographisches Institut.

HELFRICH, K. R. & MELVILLE, W. K. 2006 Long nonlinear internal waves. *Annu. Rev. Fluid Mech.* **38**, 395–425.

JACKSON, C., SILVA, J. D. & JEANS, G. 2013 Nonlinear internal waves in synthetic aperture radar imagery. *Oceanography* **26** (2), 68–79.

JIANG, S. W., KOVAČIČ, G., ZHOU, D. & CAI, D. 2019 Modulation-resonance mechanism for surface waves in a two-layer fluid system. *J. Fluid Mech.* **875**, 807–841.

KODAIRA, T., WASEDA, T., MIYATA, M. & CHOI, W. 2016 Internal solitary waves in a two-fluid system with a free surface. *J. Fluid Mech.* **804**, 201–223.

LAMB, H. 1932 *Hydrodynamics*. Cambridge University Press.

LIU, B. & HE, Y. 2016 SAR raw data simulation for ocean scenes using inverse Omega-K algorithm. *IEEE Trans. Geosci. Remote Sens.* **54** (10), 6151–6169.

MARTIN, S. 2014 *An Introduction to Ocean Remote Sensing*, 2nd edn. Cambridge University Press.

MUNK, W. H. 1950 Orgin and generation of waves. *Proc. First Conf. Coastal Engng* **1** (1), 1–4.

NARDIN, J. C., ROUSSEAUX, G. & COULLET, P. 2009 Wave–current interaction as a spatial dynamical system: Analogies with rainbow and black hole physics. *Phys. Rev. Lett.* **102** (12), 124504.

ORTIZ-SUSLOW, D. G., WANG, Q., KALOGIROS, J., YAMAGUCHI, R., PAOLO, T., TERRILL, E., SHEARMAN, R. K., WELCH, P. & SAVELYEV, I. 2019 Interactions between nonlinear internal ocean waves and the atmosphere. *Geophys. Res. Lett.* **46** (15), 9291–9299.

OSBORNE, A. R. & BURCH, T. L. 1980 Internal solitons in the Andaman Sea. *Science* **208** (4443), 451–460.

PEREGRINE, D. H. 1976 Interaction of water waves and currents. In *Advances in Applied Mechanics* (ed. C.-S. Yih), pp. 9–117. Elsevier.

PERRY, R. B. & SCHIMKE, G. R. 1965 Large-amplitude internal waves observed off the northwest coast of Sumatra. *J. Geophys. Res.* **70** (10), 2319–2324.

SCHÜTZHOLD, R. & UNRUH, W. G. 2002 Gravity wave analogues of black holes. *Phys. Rev.* D **66** (4), 044019.

SMITH, R. 1975 The reflection of short gravity waves on a non-uniform current. *Math. Proc. Camb. Phil. Soc.* **78** (03), 517–525.

STANTON, T. P. & OSTROVSKY, L. A. 1998 Observations of highly nonlinear internal solitons over the continental shelf. *Geophys. Res. Lett.* **25** (14), 2695–2698.

SUTHERLAND, B. R. 2010 *Internal Gravity Waves*. Cambridge University Press.

TANAKA, M. & WAKAYAMA, K. 2015 A numerical study on the energy transfer from surface waves to interfacial waves in a two-layer fluid system. *J. Fluid Mech.* **763**, 202–217.

WOODSON, C. B. 2018 The fate and impact of internal waves in nearshore ecosystems. *Annu. Rev. Marine Sci.* **10** (1), 421–441.

YOSHIDA, T. 2017 Azimuthal ocean wave emerged in SAR image spectra under specific condition. *J. Geophys. Res.: Oceans* **122** (12), 9625–9635.

YOUNG, I. R. 1999 *Wind Generated Ocean Waves*, 1st edn. Elsevier.

ZIEGENBEIN, J. 1969 Short internal waves in the Strait of Gibraltar. *Deep Sea Res. Oceanogr. Abstracts* **16** (5), 479–487.